

**Physics-based models of dynamic response of piezoceramics**

**Willatzen, M., Lew Yan Voon, L.C., Lassen, B., Melnik, R.**

**In: Materials Science and Technology (MS&T) 2006:**

**Materials and Systems, Volume 1, Proceedings of  
the Materials Science & Technology Conference and Exhibition,  
Duke Energy Center, Cincinnati, OH, USA, Oct 15-19, 2006,  
ISBN 978-0-470-93154-7, pp. 613--624, 2006.**

## Physics-based Models of Dynamic Response of Piezoceramics

M. Willatzen<sup>1</sup>, L. C. Lew Yan Voon<sup>2</sup>, B. Lassen<sup>1</sup>, R. Melnik<sup>3</sup>

<sup>1</sup>Mads Clausen Institute, University of Southern Denmark, Grundtvigs Allé 150, DK-6400  
Sønderborg, Denmark

<sup>2</sup>Department of Physics, Wright State University, 3640 Colonel Glenn Hwy, Dayton, OH 45435,  
USA

<sup>3</sup>Wilfrid Laurier University, 75 University Avenue West, Waterloo, Ontario N2L 3C5, Canada

Keywords: Piezoceramic transducers, nitrides, self-consistent modeling, etc.

### Abstract

A physics-based model of piezoelectric multilayer systems is presented and applied to two applications of multilayered structures. The first example is for one-dimensional multilayer ultrasound transducers, including dielectric losses in the piezoceramic material and mechanical losses in the transducer material layers. Results are shown for lead zirconate and barium titanate. The second example discusses the impact of a fully self-consistent treatment of piezoelectricity and spontaneous polarization in analyzing the device performance of nanodevices (transistors, lasers) based upon nitride wide-band-gap semiconductors. We show that different physics could be operative depending upon the material properties and device design.

### Introduction

This International Symposium focuses on Advanced Dielectric Materials and Electronic Devices. In the first area, the scope is stated to include “new materials developments/ improved properties ... for tomorrows applications.” The second area “of interest is the miniaturization of electronic devices.” In this invited paper, we present examples of what can be learned in each area through appropriate physics-based modeling as opposed to either experimental trial-and-error or through, for example, the popular equivalent electric circuit (ECC) model. The latter approach, albeit very useful for coupling to other electrical devices, suffers from not providing the details of distributions of strains, stresses, and electric fields inside the transducer and removes the user from the insight gained by working with real acoustic and electric parameters. Other drawbacks in using EEC diagrams are the difficulties in describing the details of distributed losses (acoustic) and aspects of both near-field and far-field device properties. Indeed, we have chosen to illustrate with examples for each of the two areas of interest such that there is a common originating physical model for both.

## Physical Model

The study of piezoelectric materials is a fascinating one since any type of analysis intrinsically involves solving a coupled set of differential equations representing a multiphysics problem. This level of complexity has led most to either only solve a partial problem (that we will subsequently refer to as a non-self-consistent solution) or to use equivalent electric circuit models. Our goal here is to emphasize that neither simplification is necessary and current numerical tools and hardware should allow even experimentalists to successfully and efficiently carry out accurate modeling in support of device design.

We first summarize the general piezoelectric theory under isentropic conditions; for example, this is appropriate to transducer operation under adiabatic conditions. Introducing the electric displacement  $D$ , electric field  $E$ , strain  $S$ , and stress  $T$  and using the zero point of  $D$ ,  $E$ ,  $S$ , and  $T$  as a reference value, the following set of equations can be written down under small isentropic variations [1]:

$$D_i = \left( \frac{\partial D_i}{\partial E_k} \right)_T E_k + \left( \frac{\partial D_i}{\partial T_{kl}} \right)_E T_{kl} = \epsilon_{ik}^T E_k + d_{ikl} T_{kl}, \quad (1)$$

$$E_k = \left( \frac{\partial E_k}{\partial D_i} \right)_T D_i + \left( \frac{\partial E_k}{\partial T_{lm}} \right)_D T_{lm} = \beta_{ik}^T D_i - g_{klm} T_{lm}, \quad (2)$$

$$D_i = \left( \frac{\partial D_i}{\partial E_k} \right)_S E_k + \left( \frac{\partial D_i}{\partial S_{kl}} \right)_E S_{kl} = \epsilon_{ik}^S E_k + e_{ikl} S_{kl}, \quad (3)$$

$$E_k = \left( \frac{\partial E_k}{\partial D_i} \right)_S D_i + \left( \frac{\partial E_k}{\partial S_{lm}} \right)_D S_{lm} = \beta_{ik}^S D_i - h_{klm} S_{lm}, \quad (4)$$

$$S_{kl} = \left( \frac{\partial S_{kl}}{\partial E_i} \right)_T E_i + \left( \frac{\partial S_{kl}}{\partial T_{mn}} \right)_E T_{mn} = d_{ikl} E_i + s_{klmn}^E T_{mn}, \quad (5)$$

$$T_{kl} = \left( \frac{\partial T_{kl}}{\partial E_i} \right)_S E_i + \left( \frac{\partial T_{kl}}{\partial S_{mn}} \right)_E S_{mn} = -e_{ikl} E_i + c_{klmn}^E S_{mn}, \quad (6)$$

$$S_{kl} = \left( \frac{\partial S_{kl}}{\partial D_i} \right)_T D_i + \left( \frac{\partial S_{kl}}{\partial T_{mn}} \right)_D T_{mn} = g_{ikl} D_i + s_{klmn}^D T_{mn}, \quad (7)$$

$$T_{kl} = \left( \frac{\partial T_{kl}}{\partial D_i} \right)_S D_i + \left( \frac{\partial T_{kl}}{\partial S_{mn}} \right)_D S_{mn} = -h_{ikl} D_i + c_{klmn}^D S_{mn}; \quad i, k, l, m, n = 1, 2, 3. \quad (8)$$

While it is possible to develop a full three-dimensional theory with numerical solutions, in this review, we restrict the presentation to one-dimensional models since: 1) for both applications, we will be interested in multilayers, and 2) the one-dimensional model allows for certain analytic solutions in order to make the physics clear. Thus, we will replace all the tensor components in Eqs. (1)–(8) by scalars. Indeed, for all the fields, only the “3” components remain. For the piezoelectric plate transducer, we use a thin cylinder geometry and this is the cylinder axis; thus, the transducer is operated in the thickness mode. For the multilayer heterostructure, this is the growth direction of the layers.

For dynamic response, one can now derive wave equations. In particular, Newton’s Second Law, Poisson’s Law, and the definition of strain together with the appropriate mechanical boundary conditions and subsidiary electromechanical conditions (e.g., the coupling between applied voltage and electric displacement, transducer electrode velocities) completely determine the temporal and spatial behavior of the resulting strains, stresses, velocities, currents, and voltages in the device.

Application of Newton's Second Law leads to the Navier equation:

$$\nabla \cdot \mathbf{T} = \rho_d \frac{\partial^2 \mathbf{u}}{\partial t^2}, \quad (9)$$

and Poisson's equation is

$$\nabla \cdot \mathbf{D} = \rho_f, \quad (10)$$

where  $\mathbf{u} = (u_x, u_y, u_z)$  is the particle displacement. The coefficients  $\rho_d$ , and  $\rho_f$  denote the position-dependent mass density and the free-charge carrier density, respectively.

The corresponding wave equations for the one-dimensional (spatial) problem are

$$\frac{\partial^2 u}{\partial t^2} - v_a^2 \frac{\partial^2 u}{\partial z^2} = 0, \quad (11)$$

$$\frac{\partial^2 S}{\partial t^2} - v_a^2 \frac{\partial^2 S}{\partial z^2} = 0, \quad (12)$$

where  $v_a = \sqrt{\frac{c^D}{\rho_d}}$  is the layer-dependent sound velocity, i.e., it depends on the position coordinate  $z$  for a multilayer structure. General harmonic solutions can be written down:

$$u = u_A \exp(-ikz - i\omega t) + u_B \exp(ikz - i\omega t), \quad (13)$$

$$S = S_A \exp(-ikz - i\omega t) + S_B \exp(ikz - i\omega t). \quad (14)$$

If we now impose the appropriate boundary conditions, a system of coupled linear equations result. At this point, it is necessary to specify the physical problem being solved.

### Application: Piezoceramic Transducers

The multilayer structure is chosen to consist of a piezoceramic material (thickness  $l_{pz}$ ), an acoustic coupling layer (e.g., grease, thickness  $l_{ac}$ ), and a matching layer (thickness  $l_{ma}$ ). To simplify the model, we have neglected the thicknesses of the plate electrode layers in this example but the arguments involved can easily be extended to any multilayer transducer consisting of an arbitrary number of layers and thicknesses.

Imposing continuity of the (normal) velocity and pressure between layers/surrounding media yield nine equations in nine unknowns for the multilayer transmitter structure depicted in Fig. 1(a). The unknowns are:  $D, T_L, T_R, S_{A_i}, S_{B_i}, i = 1, 2, 3$  where  $T_L$  and  $T_R$  refer to the stress amplitude associated with the backward-propagating wave  $L$  (in air) and the forward-propagating stress wave  $R$  (in water), respectively. The nine equations are given in Table 1.  $c_m^D, Z_{am}, k_m, h_m, \epsilon_m^S$  are the bulk modulus under constant electric displacement, acoustic impedance, wave vector, piezoelectric  $h$  constant, permittivity under constant strain of layer  $m$ , respectively, and  $Z_{aR}$  ( $Z_{aL}$ ) is the acoustic impedance of the medium located right (left) to the transducer. Recall that layer 1, layer 2, and layer 3 in the case of the transmitter are the piezoceramic layer, the acoustic coupling layer, and the matching layer, respectively, so that, e.g.,  $l_1, l_2$ , and  $l_3$  are equal to  $l_{pz}, l_{ac}$ , and  $l_{ma}$ , respectively.

The geometry and material structure of the receiver [Fig. 1(b)] is the same as for the transmitter (reciprocal transducer setup), however, the input signal is now the incoming pressure signal (designated  $T_i$ ) from the transmitter which induces an electric displacement in the receiver piezoceramic

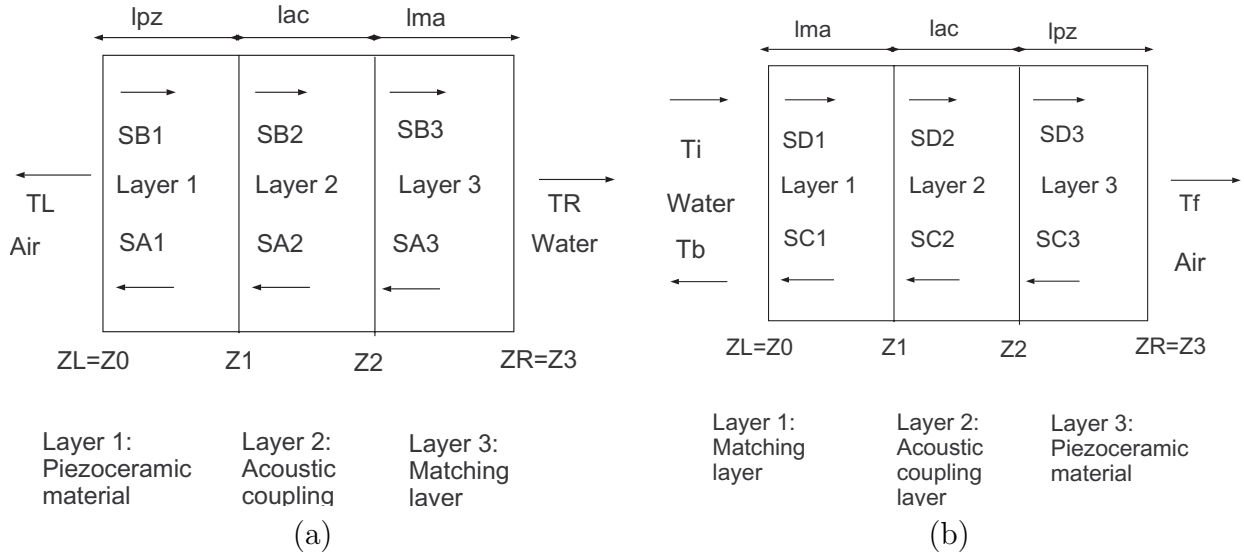


Figure 1: (a) Transmitter and (b) receiver geometry.

material equivalent to a receiver current and (through the transducer impedance) a receiver voltage. The procedure for determining the unknown receiver parameters is similar to the procedure described above for the transmitter.

Numerical results for different transducer designs are now presented in order to illustrate the model. Three common ultrasound transducers are considered: a) a “pure” piezoceramic transducer, i.e., a transducer consisting of the piezoceramic material only, without any matching layer, b) a transducer consisting of a piezoceramic material and a quarter-wavelength matching layer of the commonly used material: Polyphenylsulfide (PPS) [PPS is characterized by an acoustic impedance value close to the geometric mean of the acoustic impedances of the piezoceramics and water], and c) a transducer consisting of a piezoceramic layer and a half-wavelength matching layer of stainless steel. To simplify matters, acoustic coupling layers between the piezoceramics and matching layers are disregarded.

We choose the excitation voltage  $V(t)$  of the form shown in Fig. 2(a), i.e., a sinusoidal voltage pulse consisting of eight periods with a driving frequency of 1 MHz. The resulting Fourier transform of the voltage pulse is shown in Fig. 2(b). In the following, focus will be on voltage signals generated in the receiver. Additional results on the current and both near-field and far-field responses have been previously reported [1]. It is also assumed that the transmitter and receiver are identical, i.e., the ultrasound system is reciprocal. All calculations and figures include dielectric and mechanical losses if nothing else is stated.

In Fig. 3, we compare the receiver signal for the three configurations. In Fig. 3(a), the voltage pulse across the electrode layers of the “pure” piezoceramic transducer is shown. The maximum voltage is obtained after approximately eight cycles. The signal front rises steeply to the pulse maximum value after which the signal falls down to zero in a short time. Such a transducer signal is convenient for electronic detection purposes as a steep front-edge rising facilitates determination of pulse arrival times. Losses lead to a pulse amplitude decrease of about 15 %. In Fig. 3(b), the received voltage pulse is shown for a transducer consisting of the piezoceramic layer and a quarter-wavelength matching layer of PPS. The peak maximum voltage is some 20 % above that

Table 1: Transducer dynamic equations in Fourier representation [1].

$$\begin{aligned}
T_L &= c_1^D (S_{A_1} + S_{B_1}) - h_1 D \\
\frac{T_L}{Z_{aL}} &= c_1^D \left( \frac{S_{A_1}}{Z_{a1}} - \frac{S_{B_1}}{Z_{a1}} \right) \\
c_2^D (S_{A_2} + S_{B_2}) &= c_1^D (S_{A_1} \exp(-ik_1 l_1) + S_{B_1} \exp(ik_1 l_1)) \\
&\quad - h_1 D \\
c_2^D \left( \frac{S_{A_2}}{Z_{a2}} - \frac{S_{B_2}}{Z_{a2}} \right) &= c_1^D \left( \frac{S_{A_1} \exp(-ik_1 l_1)}{Z_{a1}} - \frac{S_{B_1} \exp(ik_1 l_1)}{Z_{a1}} \right) \\
c_3^D (S_{A_3} + S_{B_3}) &= c_2^D (S_{A_2} \exp(-ik_2 l_2) + S_{B_2} \exp(ik_2 l_2)) \\
c_3^D \left( \frac{S_{A_3}}{Z_{a3}} - \frac{S_{B_3}}{Z_{a3}} \right) &= c_2^D \left( \frac{S_{A_2} \exp(-ik_2 l_2)}{Z_{a2}} - \frac{S_{B_2} \exp(ik_2 l_2)}{Z_{a2}} \right) \\
T_R &= c_3^D (S_{A_3} \exp(-ik_3 l_3) + S_{B_3} \exp(ik_3 l_3)) \\
-\frac{T_R}{Z_{aR}} &= c_3^D \left( \frac{S_{A_3} \exp(-ik_3 l_3)}{Z_{a3}} - \frac{S_{B_3} \exp(ik_3 l_3)}{Z_{a3}} \right) \\
-i\omega V &= -AZ_{e1}\omega^2 D - i\omega \frac{l_1}{\epsilon_1 S} D - h_1 \left[ c_2^D \left( \frac{S_{A_2}}{Z_{a2}} - \frac{S_{B_2}}{Z_{a2}} \right) - c_1^D \left( \frac{S_{A_1}}{Z_{a1}} - \frac{S_{B_1}}{Z_{a1}} \right) \right],
\end{aligned} \tag{15}$$

of the voltage signal shown in Fig. 3(a). Again, the front-edge of the pulse rises steeply (maximum after four periods) followed by a fast pulse extinction. In Fig. 3(c), the receiver voltage pulse corresponding to a piezoceramic transducer with a half-wavelength matching layer of stainless steel is depicted. It is evident that this signal does not show the same positive characteristics in terms of maximum pulse voltage value, front-edge rising, and fast extinction of transducer reverberations, as seen in the two previous cases: the pulse in Fig. 3(c) reaches its maximum value after 9–11 cycles and continues to oscillate for much longer times as compared to the two previous receiver pulses. This behavior can be understood in the following way: Although energy is not added to the transducer after the first eight cycles [Fig. 3(c)], energy is still added to the steel a few cycles after the electrical excitation ceases. This time delay is due to a slow energy transport from the piezoceramics into steel. Although the transmission intensity coefficient for sound transmission from a semi-infinite layer of piezoceramics into water through a half-wavelength matching layer of steel is equal to the

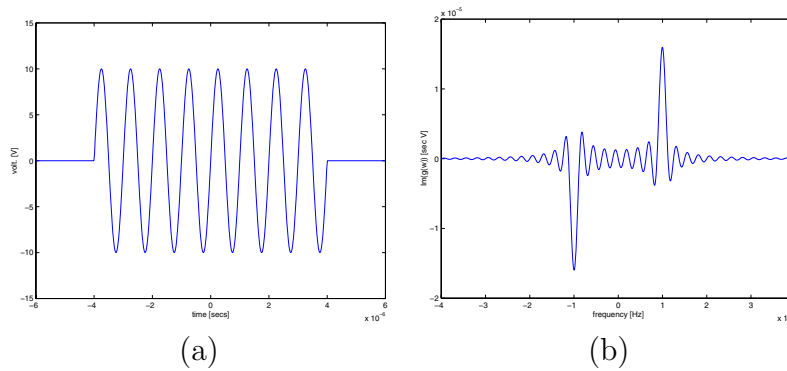


Figure 2: (a) Excitation voltage. (b) Fourier transform.

corresponding sound intensity transmission coefficient for transmission directly into water from a semi-infinite layer of piezoceramics at the driving frequency and at integral multiples of the driving frequency, the signal characteristics are somewhat deteriorated in terms of amplitude and time for reverberations to die out. Again, apart from not having a semi-infinite piezoceramic layer, this is due to reduced transmission at all other frequencies present in the excitation voltage pulse in the case of a transducer with a half-wavelength matching layer of stainless steel as compared to the case of a “pure” piezoceramic transducer.

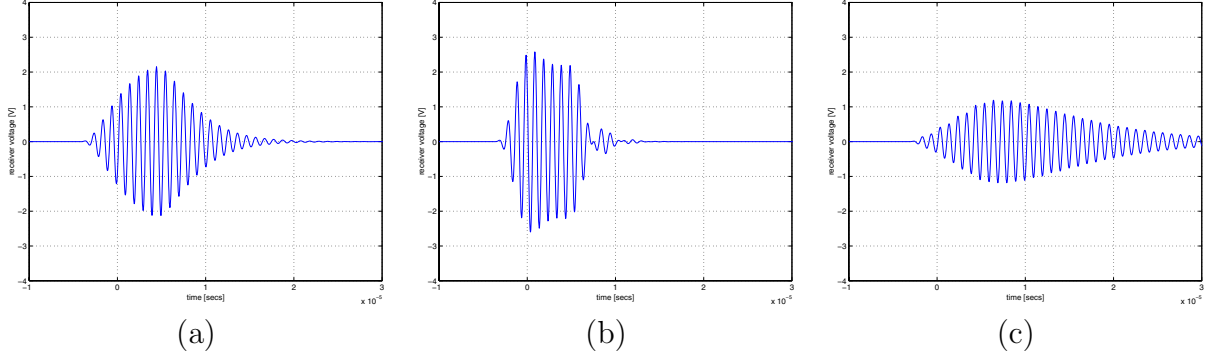


Figure 3: Receiver voltage pulses due to the excitation pulse shown in Fig. 2(a) for the cases a) “pure” piezoceramic transducer without matching layers; b) piezoceramic transducer with a quarter-wave matching layer of PPS; and, c) piezoceramic transducer with a half-wavelength matching layer of stainless steel. Adapted from Ref. [1].

In order to illustrate the flexibility of the model, we now present results of similar calculations for a  $\text{BaTiO}_3$  reciprocal transducer setup.  $\text{BaTiO}_3$  has traditionally a strong place among materials used for piezoelectric applications although PZT materials recently largely replace  $\text{BaTiO}_3$  materials (the two materials have similar piezoelectric coupling coefficients but PZT materials is mechanically more stable and show a larger dielectric constant). The data used in the computations are the following:  $\rho_d = 5700 \text{ kg}/(\text{m}^3)$ ,  $c_d = 14.6 \cdot 10^{10} \text{ N}/\text{m}^2$ ,  $\epsilon = 1260\epsilon_0$ ,  $\epsilon_0 = 8.854 \cdot 10^{-12} \text{ F}/\text{m}$ ,  $h = 17.5/\epsilon$  [in the latter expression the unit of  $h$  is in  $\text{C}/\text{m}$  when  $\epsilon$  is in  $\text{F}/\text{m}$ ]. The thickness of the  $\text{BaTiO}_3$  layer is chosen to be a half-wavelength at 1 MHz equivalent to 0.00253 m. In Fig. 4, the transmitter generator voltage is shown as a function of time. The voltage input is a two-period sinus-burst at 1 MHz of amplitude 10 V. Three receiver-voltage signals are shown in Fig. 5 subject to the excitation voltage in Fig. 4 corresponding to the case (a) where a single-piezoceramic layer of  $\text{BaTiO}_3$  is in series with a resistor of  $100 \Omega$  in both the transmitter and receiver circuits, (b) where the resistor of  $100 \Omega$  is removed from the transmitter and receiver circuits, and (c) the case where the piezoceramic layer is coupled to a steel matching layer (with similar acoustic data as in Ref. [1]) including the  $100 \Omega$  in both the transmitter and receiver circuits. Evidently the presence of the resistor leads to a smaller receiver voltage but also a shorter time-duration signal (which is often preferable in applications). The inclusion of a steel matching layer leads to a further deterioration of the signal amplitude but, again in some applications, this is acceptable since the steel layer protects the piezoceramic layer from mechanical wear and increases the robustness subject to hostile-environment applications.

In Fig. 6, the voltage excitation signal for an eight-period sinus burst is shown again corresponding to a driving frequency of 1 MHz and amplitude 10 V. The three receiver-voltage signals corresponding to this excitation voltage are shown in Fig. 7 for the same cases with and without a resistor and a steel matching layer as shown in Fig. 5. Evidently, applying a longer-duration sinus burst leads

to a significant increase in the receiver-voltage amplitudes which are often beneficial (improves the signal-to-noise ratio).

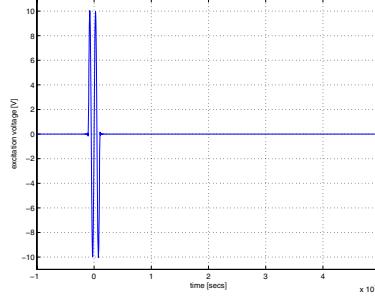


Figure 4: BaTiO<sub>3</sub> — two-period sinus burst input voltage excitation.

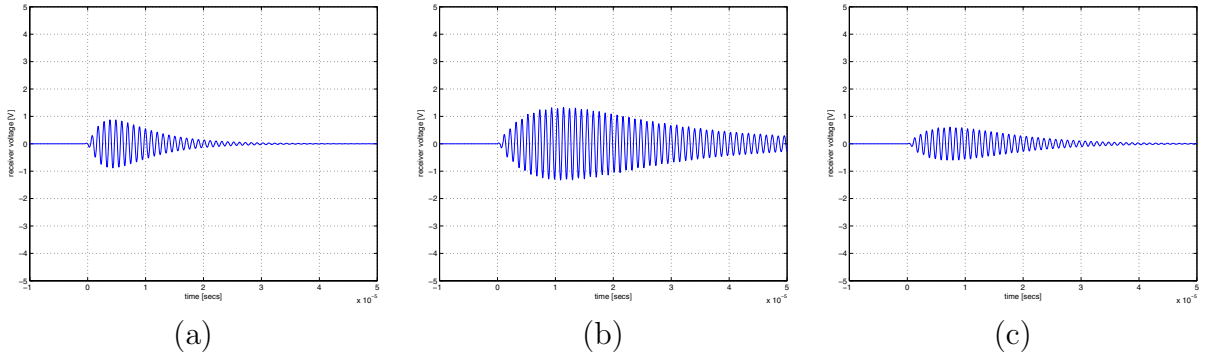


Figure 5: BaTiO<sub>3</sub> reciprocal transducer setup. Receiver-voltage signals for a BaTiO<sub>3</sub> piezoceramic transducer (a) coupled to a 100  $\Omega$  resistor, (b) without a series resistor, and (c) coupled to a 100  $\Omega$  resistor and acoustically coupled to a steel matching layer. Signals correspond to the input voltage shown in Fig. 4.

### Application: Wurtzite Multilayered Nanostructures

Wurtzite-based nanostructures have been receiving a lot of attention for high-temperature, high-power, high-frequency, and optical applications. The presence of built-in strain in a multilayer structure leads to internal piezoelectric fields that have significant impact on the physical properties. In addition, the inhomogeneous structures introduce an additional spontaneous polarization contribution. Current models of such behaviour for both transistor and optoelectronic devices have been incomplete and apparently contradictory.

We first extend the above piezoelectric theory to account for the situation relevant to strained heterostructures. The strain  $\mathbf{S}$  accounts for lattice mismatch and is defined by [2]:

$$\begin{aligned} S_1 &= \frac{\partial u_x}{\partial x} - \frac{a(\vec{r}) - a^{(1)}}{a^{(1)}}, & S_4 &= \frac{1}{2} \left( \frac{\partial u_y}{\partial z} + \frac{\partial u_z}{\partial y} \right), \\ S_2 &= \frac{\partial u_y}{\partial y} - \frac{a(\vec{r}) - a^{(1)}}{a^{(1)}}, & S_5 &= \frac{1}{2} \left( \frac{\partial u_x}{\partial z} + \frac{\partial u_z}{\partial x} \right), \end{aligned} \quad (16)$$



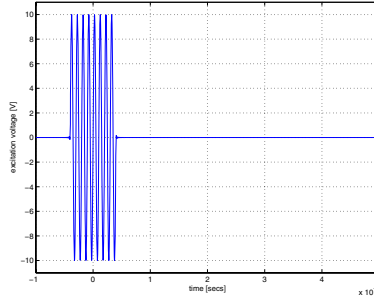


Figure 6: BaTiO<sub>3</sub> — eight-period sinus burst input voltage excitation.

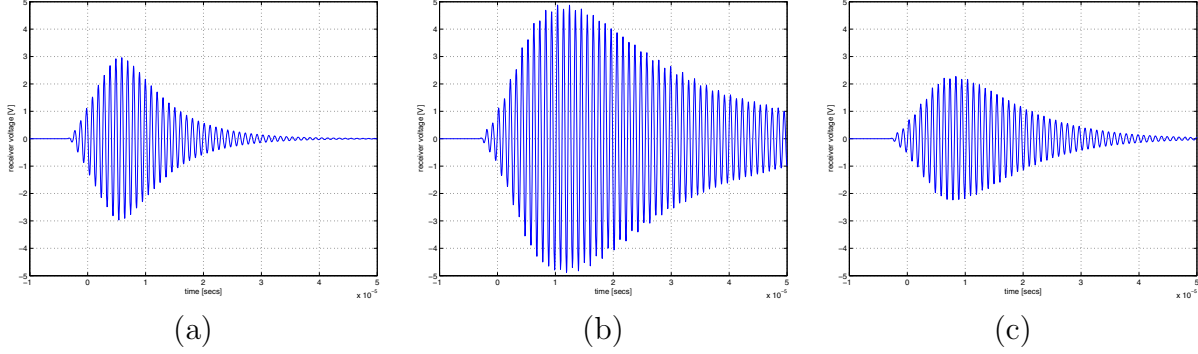


Figure 7: BaTiO<sub>3</sub> reciprocal transducer setup. Receiver-voltage signals for a BaTiO<sub>3</sub> piezoceramic transducer (a) coupled to a 100  $\Omega$  resistor, (b) without a series resistor, and (c) coupled to a 100  $\Omega$  resistor and acoustically coupled to a steel matching layer. Signals correspond to the input voltage shown in Fig. 6.

$$S_3 = \frac{\partial u_z}{\partial z} - \frac{c(\vec{r}) - c^{(1)}}{c^{(1)}}, \quad S_6 = \frac{1}{2} \left( \frac{\partial u_x}{\partial y} + \frac{\partial u_y}{\partial x} \right),$$

where  $a(\vec{r})$ ,  $c(\vec{r})$  are the lattice constants at position  $\vec{r}$  while  $a^{(1)}$ ,  $c^{(1)}$  denote the lattice constants of the barrier material.

Recent calculations of the electronic states in wurtzite AlN/GaN quantum dots [3, 4] have ignored the fully-coupled model of the piezoelectric effect. Nevertheless, there are conflicting results regarding the need for such a model even for one-dimensional structures [5, 6]. Thus, Jogai *et al.* [5] showed that the internal electric field can be as high as 5 MV/cm for AlGaIn/GaN quantum-well structures and, consequently, the difference between a full-coupled model and a semi-coupled model can be as high as 60 %. On the other hand, calculations just published by Christmas *et al.* [6] found only a 2 % error in the internal fields for InGaIn/GaN using the two models; yet, they did not comment on the significance of this new result. In order to compare the above work, we have, therefore, introduced an analytical model where we generalize the above work to include internal fields in both layers. Furthermore, we point out all of the above-referenced work were performed under static conditions while many applications (e.g., laser diodes) would require AC response; hence, we also consider the latter case here.

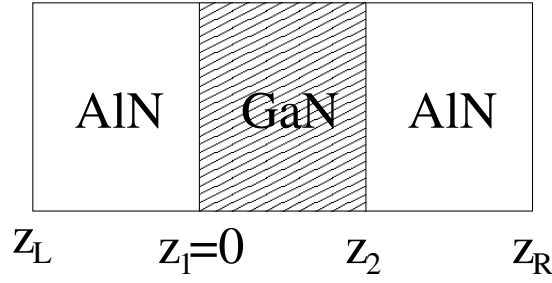


Figure 8: Schematics of a typical three-layer quantum-well structure considered in the present work.

### Static properties

While this paper focusses on dynamic properties, we present a brief review of recent results on static properties that has clarified the role of the various phenomena in determining the internal piezoelectric fields. Details will be published elsewhere.

In a fully-coupled model, the internal fields can also influence the strain distribution via the indirect effect, one not taken into consideration by Fonoberov *et al.* [3, 4] In this case, our equations reduce to Eq. (15) of Jogai *et al.* [5] and to Eqs. (12)–(13) of Christmas *et al.* [6] in the appropriate limits. The most transparent form is that of Jogai *et al.* [5] which we rewrite below as (without the 2D electron gas)

$$S_3 = -\frac{2c_{13}^{(1)}}{c_{33}^{(1)}}S_1 + \left[ \frac{2e_{33}^{(1)}(e_{33}^{(1)}c_{13}^{(1)} - e_{13}^{(1)}c_{33}^{(1)})}{c_{33}^{(1)}(\epsilon_{||,1}c_{33}^{(1)} + e_{33}^{(1)2})} \right] S_1 + \frac{e_{33}^{(1)}(P^{\text{sp,GaN}} - P^{\text{sp,1}})}{\epsilon_{||,1}c_{33}^{(1)} + e_{33}^{(1)2}} \quad (17)$$

$$\equiv S_{\text{uncoupled}} + S_{\text{coupled}} + S_{\text{spon}}, \quad (18)$$

where we have labeled the three strain terms according to their origin.

The relative magnitude of the three strain contributions are given in Table 2 for four material compositions: AlN/GaN, Al<sub>0.3</sub>Ga<sub>0.7</sub>N/GaN, In<sub>0.2</sub>Ga<sub>0.8</sub>N/GaN, and ZnO/Zn<sub>0.8</sub>Mg<sub>0.2</sub>O. Table 2 shows that the relative difference between an uncoupled and a coupled calculation is of order 18%, 9%, 6% and 20% for AlN, AlGa<sub>0.3</sub>N, InGa<sub>0.2</sub>N, and ZnO, respectively. Spontaneous polarization contribution adds another 18%, 14%, 0.7%, and 10%. This analysis explains the apparent contradiction between the results of Jogai *et al.* [5] and Christmas *et al.* [6] Thus, the extremely large coupling reported by Jogai *et al.* [5] for AlGa<sub>0.3</sub>N is here seen to be, in fact, due to both the spontaneous polarization term and the coupling term. For pure AlN, the last two contributions are of equal magnitude if GaN is the substrate (as is often the case in a QW structure), and similarly for ZnO on ZnMgO. For InGa<sub>0.2</sub>N, the situation is reversed whereby the spontaneous polarization almost does not contribute; hence, the relatively smaller difference in strain reported by Christmas *et al.* [6] is almost entirely due to the difference between the coupled and uncoupled models. In conclusion, the relative importance of the fully-coupled model is strongly dependent upon the material system under investigation and spontaneous polarization may or may not be neglected.

## Dynamic properties

Preliminary results on the dynamic properties have recently been obtained. The interest here lies in the result that there exists resonance frequencies at which the strain distributions are strongly affected by the piezoelectric coupling, more so than in the static case presented above.

For the case of a single piezoceramic layer of GaN with vacuum environments at  $z = 0$  and  $z = l$ , the stress equations formulated in the strain coefficients read:

$$c'_{33} (S_A + S_B) - \frac{e_{33}}{\epsilon} D = 0, \quad (19)$$

$$c'_{33} (S_A \exp(-ikl) + S_B \exp(ikl)) - \frac{e_{33}}{\epsilon} D = 0, \quad (20)$$

with  $c'_{33} = c_{33} + e_{33}^2/\epsilon_{33}$ . They can be solved for  $k$  so as to obtain the resonance conditions (infinite strain coefficients in the case of no losses). The result is:

$$kl = (2n + 1)\pi, \quad (21)$$

with  $n$  an integer. Hence, the resonance frequencies are:

$$f = \frac{\omega}{2\pi} = \frac{(2n + 1)}{2l} \sqrt{\frac{c'_{33}}{\rho_d}}. \quad (22)$$

We consider next the case of a GaN quantum well sandwiched between two layers of AlN. In Fig. 9, we give the first three resonance frequencies for the three-layer structure with AlN layer lengths  $l_1 = l_3 = 1 \cdot 10^{-7}$  while the GaN layer length  $l_2$  varies in the range  $2.5 \cdot 10^{-9} - 30 \cdot 10^{-9}$ . We use values for the mass density of AlN ( $\rho_d^{(1)} = 3260$ ) [9] and GaN ( $\rho_d^{(2)} = 6150$ ) [10]. The precise values of the strain coefficients  $S_{A_i}, S_{B_i}$  for a given current near resonances are albeit large not infinite due to acoustic and dielectric losses present in the system.

## Summary

The complete self-consistent equations for the piezoelectric field and spontaneous polarization are presented and used to solve two multilayer problems. It is shown how insight into the physics can be thus derived. The transducer model should be useful for modeling and designing devices operating in the thickness mode. The nanostructure model is useful for identifying the physical origins and for calculating the magnitude of the internal fields. These can then be used for device (for example, transistors and lasers) simulation.

## Acknowledgments

The work was supported by a Research Challenge grant from Wright State University and the Ohio Board of Regents.

Table 2: Contributions to the vertical strain. Parameters are taken from Jogai *et al.* [5] and Christmas *et al.* [6] for the nitrides, and from Park *et al.* [7] and Gopal and Spaldin [8] for the oxides.

	$S_{\text{uncoupled}}$	$S_{\text{coupled}}$	$S_{\text{spon}}$
AlN/GaN	−0.0143	0.0026	0.0026
Al <sub>0.3</sub> Ga <sub>0.7</sub> N/GaN	−0.0039	0.0004	0.0005
In <sub>0.2</sub> Ga <sub>0.8</sub> N/GaN	0.0119	−0.0008	0.0001
ZnO/Zn <sub>0.8</sub> Mg <sub>0.2</sub> O	0.0032	−0.0006	−0.0003

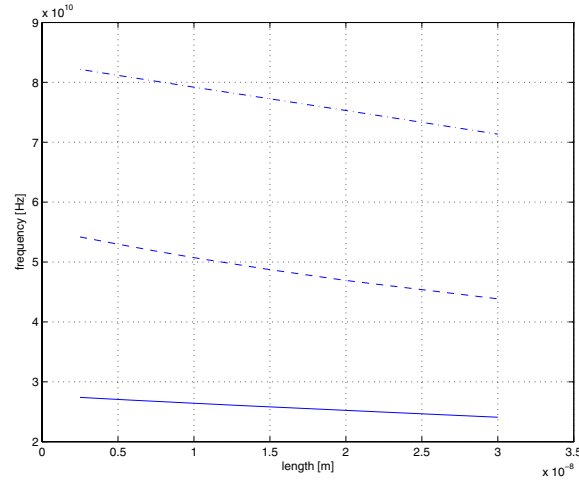


Figure 9: Resonance frequencies of a three-layer system corresponding to one layer of GaN sandwiched between two layers of AlN. The figure shows the first three resonance frequencies (solid, dashed, and dash-dotted curves) as a function of the GaN material-layer lengths. The two AlN layers have the same length equal to  $1 \cdot 10^{-8}$  independent of the GaN material-layer length. Figure values are in SI units.

## References

- [1] M. Willatzen. Ultrasound transducer modeling — General theory and applications to ultrasound reciprocal systems. *IEEE Trans. Ultrasonics Ferroelectrics Freq. Con.* **48**, 100 (2001).
- [2] I. P. Ipatova, V. G. Malyskin, and V. A. Shchukin. On spinodal decomposition in elastically anisotropic epitaxial films of III-V semiconductor alloys. *J. Appl. Phys.* **74**, 7198 (1993).
- [3] V. A. Fonoberov and A. A. Balandin. Excitonic properties of strained wurtzite and zinc-blende GaN/Al<sub>x</sub>Ga<sub>1-x</sub>N quantum dots. *J. Appl. Phys.* **94**, 7178 (2003).
- [4] V. A. Fonoberov and A. A. Balandin. Optical properties of wurtzite and zinc-blende GaN/AlN quantum dots. *J. Vac. Sci. Tech.* **22**, 2190 (2004).
- [5] B. Jogai, J. D. Albrecht, and E. Pan. Effect of electromechanical coupling on the strain in AlGaIn/GaN heterojunction field effect transistors. *J. Appl. Phys.* **94**, 3984 (2003).
- [6] Ursula M. E. Christmas, A. D. Andreev, and D. A. Faux. Calculation of electric field and optical transitions in InGaIn/GaN quantum wells. *J. Appl. Phys.* **98**, 073522 (2005).
- [7] Seoung-Hwan Park, Kwang Joo Kim, Sam Nyung Yi, Doyeol Ahn, and Seung Joo Lee. ZnO/MgZnO quantum well lasers for optoelectronic applications in the blue and the UV spectral regions. *J. Korean Phys. Soc.* **47**, 448 (2005).
- [8] Priya Gopal and Nicola Spaldin. Polarization, piezoelectric constants and elastic constants of ZnO, MgO and CdO. *cond-mat/0507217*.
- [9] G. A. Slack. Nonmetallic crystals with high thermal conductivity. *J. Phys. Chem. Solids* **34**, 321 (1973).
- [10] J. C. Cao and X. L. Lei. Nonparabolic multivalley balance-equation approach to impact ionization: application to wurtzite GaN. *Eur. Phys. J. B* **7**, 79 (1999).